

## Collective excitations in three-dimensional Dirac systems

Q. N. Li<sup>1,2</sup>, P. Vasilopoulos,<sup>3</sup> F. M. Peeters<sup>2,4,5</sup>, W. Xu,<sup>1,5,6,\*</sup> Y. M. Xiao<sup>1,†</sup> and M. V. Milošević<sup>2,‡</sup>

<sup>1</sup>*School of Physics and Astronomy and Yunnan Key Laboratory of Quantum Information, Yunnan University, Kunming 650091, China*

<sup>2</sup>*Department of Physics, University of Antwerp, Groenenborgerlaan 171, B-2020 Antwerpen, Belgium*

<sup>3</sup>*Department of Physics, Concordia University, 7141 Sherbrooke St. W. Montreal, Canada*

<sup>4</sup>*Departamento de Física, Universidade Federal do Ceará, 60455-760 Fortaleza, Ceará, Brazil*

<sup>5</sup>*Micro Optical Instruments Inc., Shenzhen 518118, China*

<sup>6</sup>*Key Laboratory of Materials Physics, Institute of Solid State Physics, HFIPS, Chinese Academy of Sciences, Hefei 230031, China*



(Received 13 December 2023; revised 24 January 2024; accepted 20 February 2024; published 13 March 2024)

We provide the plasmon spectrum and related properties of the three-dimensional (3D) Dirac semimetals  $\text{Na}_3\text{Bi}$  and  $\text{Cd}_3\text{As}_2$  based on the random-phase approximation. The necessary one-electron eigenvalues and eigenfunctions are obtained from an effective  $\mathbf{k} \cdot \mathbf{p}$  Hamiltonian. Below the energy at which the velocity  $v_z$  along the  $k_z$  axis vanishes, the density of states differs drastically from that of a 3D electron gas (3DEG) or graphene. The dispersion relation is anisotropic for wave vectors parallel ( $q$ ) and perpendicular ( $q_z$ ) to the  $(x, y)$  plane and is markedly different than that of graphene or a 3DEG. The same holds for the energy-loss function. Both depend sensitively on the position of the Fermi energy  $E_F$  relative to the region of the Berry curvature of the bands. For  $E_F$  below the energy at which  $v_z$  vanishes, the range of the relevant wave vectors  $q$  and  $q_z$  shrinks, for  $q_z$  by about one order of magnitude.

DOI: [10.1103/PhysRevB.109.115123](https://doi.org/10.1103/PhysRevB.109.115123)

### I. INTRODUCTION

In the last decade, three-dimensional (3D) Dirac semimetals (DSMs), in which doubly degenerate conduction and valence bands cross linearly at one or more Dirac points, have been studied extensively [1–8]. The electronic dispersion relation of the low-energy excitations around the Dirac points is linear and resembles the massless Dirac equation of relativistic particle physics. In particular, it has been found that  $\text{Na}_3\text{Bi}$  and  $\text{Cd}_3\text{As}_2$  are 3D DSMs that have two symmetry Dirac points connected by a pair of opposite chiral Fermi arcs [4,6].

Angle-resolved photoemission spectroscopy (ARPES) experiments have unveiled a pair of stable 3D bulk Dirac points in both  $\text{Na}_3\text{Bi}$  and  $\text{Cd}_3\text{As}_2$ , located on opposite sides of the Brillouin zone center ( $\Gamma$  point) which are protected by crystal symmetries [4–8]. The Fermi arc surface state, Berry curvatures, and anisotropic energy dispersions are observed as well in their 3D energy bands, which is in line with theoretical predictions [4,6]. This unique energy dispersion of 3D DSMs leads to many interesting properties, such as ultrahigh carrier mobilities [9–11], chiral anomalies [12,13], topological phase transitions [14,15], ultrafast transient times [16], nonlinear optical responses [17,18], quantum Hall effect in thin films [19], and in the bulk [20]. Reviews of their properties, as well as those of Weyl semimetals, can be found in Refs. [21,22].

Despite the strong research activity in DSMs, we find that their collective excitations have not been studied as extensively as other properties. We are aware only of the studies of

Ref. [23] for  $\text{Na}_3\text{Bi}$  and  $\text{Cd}_3\text{As}_2$ , of Refs. [24,25] for general 3D DSMs, and of Ref. [26] for  $\text{PtTe}_2$ . In all of them, only limited aspects of these excitations have been studied with very simplified energy spectra that are valid only very close to the Dirac points. In particular, Ref. [24] used the spectrum  $E_{\mathbf{k},s} = s\hbar v_F \mathbf{k}$ , where  $\mathbf{k}$  is the 3D momentum,  $v_F$  is the Fermi velocity, and  $s$  the band index. This spectrum was criticized in Ref. [21]. Transport studies of 3D DSMs indicate that the simple energy spectra cannot explain their electronic excitations well due to their unique electronic band structures, so their plasmon modes remain unclear [10,11].

The aim of this paper is to present a comprehensive random-phase approximation (RPA) treatment of collective excitations in  $\text{Na}_3\text{Bi}$  and  $\text{Cd}_3\text{As}_2$  using the broadly accepted energy spectrum of the  $\mathbf{k} \cdot \mathbf{p}$  approximation [2,3], i.e., without unnecessary simplifications, and present a full account of the plasmon spectrum and of the corresponding energy loss. Using the energy band structures of 3D DSMs, we found that their collective excitations are anisotropic and sensitively affected by the Berry curvature of the bands. This is in sharp contrast to graphene or other 3D systems like layered graphene [27], Weyl semimetals [28], and 3D DSMs with isotropic Dirac cones [26].

The paper is organized as follows. In Sec. II, we present the basics of the one-electron aspects and in Sec. III the relevant dielectric functions. In Sec. IV, we present our results and discussion, and in Sec. V our summary.

### II. ONE-ELECTRON ASPECTS

$\text{Na}_3\text{Bi}$  is a hexagonal crystal normally in its  $P6_3/mmc$  or  $D_{6h}^4$  phase. There are two nonequivalent Na sites noted as Na(1) and Na(2). Na(1) and Bi can form simple honeycomb

\*wexu\_issp@aliyun.com

†yiming.xiao@ynu.edu.cn

‡milorad.milosevic@uantwerpen.be

lattice layers stacked along the  $c$  axis. The Na(2) atoms are sandwiched between the above-mentioned lattice layers and connect to the Bi atoms in forming the layers of honeycomb lattices. Na<sub>3</sub>Bi has an inverted band structure and its Fermi surface consists of two isolated Fermi points [2]. Both time-reversal and inversion symmetries are present in Na<sub>3</sub>Bi, so there is fourfold degeneracy at each Fermi point around which the band dispersion can be linearized. Due to the lattice structure, asymmetric features of the electronic band structure are expected for Na<sub>3</sub>Bi Dirac fermions. In the  $\mathbf{k} \cdot \mathbf{p}$  approximation [2], the Hamiltonian for low-energy electrons is given by

$$H(\mathbf{K}) = \epsilon_{\mathbf{K}} \times I + \begin{pmatrix} M_{\mathbf{K}} & Ak_+ & 0 & B_{\mathbf{K}}^* \\ Ak_- & -M_{\mathbf{K}} & B_{\mathbf{K}}^* & 0 \\ 0 & B_{\mathbf{K}} & M_{\mathbf{K}} & -Ak_- \\ B_{\mathbf{K}} & 0 & -Ak_+ & -M_{\mathbf{K}} \end{pmatrix}, \quad (1)$$

where  $\mathbf{K} = (\mathbf{k}, k_z) = (k_x, k_y, k_z)$  is the electron wave vector or momentum operator, and  $I$  is the  $4 \times 4$  unitary matrix. The  $z$  axis is the direction of stacking honeycomb lattice layers to form Na(1) and Bi. Further,  $k_{\pm} = k_x \pm ik_y$ ,  $\epsilon_{\mathbf{K}} = C_0 + C_1 k_z^2 + C_2 k^2$ ,  $M_{\mathbf{K}} = M_0 - M_1 k_z^2 - M_2 k^2$ , and  $C_0$ ,  $C_1$ ,  $C_2$ ,  $M_0$ ,  $M_1$ ,  $M_2$ , and  $A$  are band parameters [2,29]. In Eq. (1),  $B_{\mathbf{K}} = B_3 k_z k_{\pm}^2 \sim K^3$  gives a high-order contribution to the electron motion, which is significant only at relatively large electron momentum. The corresponding Schrödinger equation can be solved analytically and the eigenvalues obtained are  $E_{\pm}(\mathbf{K}) = \epsilon_{\mathbf{K}} \pm [M_{\mathbf{K}}^2 + A^2 k^2 + |B_{\mathbf{K}}|^2]^{1/2}$ , where the  $+$  ( $-$ ) sign refers to the conduction (valence) band. There exist two Dirac points at  $k = 0$  and  $k_z = \pm k_c = \pm[M_0/M_1]^{1/2}$ ; see Fig. 1.

ARPES and spin-resolved ARPES measurements indicate that the energy bands for both Na<sub>3</sub>Bi and Cd<sub>3</sub>As<sub>2</sub> are spin degenerate near the Dirac points [4,7] and the observable energy band splitting occurs in large energy and high magnetic field ranges [30]. These experimental works are in good agreement with theoretical predictions for Na<sub>3</sub>Bi and Cd<sub>3</sub>As<sub>2</sub> [2,3]. The plasmons, induced by electron-electron (e-e) interactions, mainly occur in low-energy and small-momentum regimes, in which case a spin degeneracy occurs. Thus, we can neglect the high-order terms containing  $B_{\mathbf{K}}$  in Eq. (1). The  $4 \times 4$  matrix becomes block diagonal in form with two  $2 \times 2$  matrices, the upper-left block  $H_u(\mathbf{K})$ , and lower-right block  $H_l(\mathbf{K})$ , respectively. By time reversal symmetry of 3D DSMs, we have  $H_l(\mathbf{K}) = H_u^*(-\mathbf{K})$  [21]. This allows us to focus on studying the  $H_u(\mathbf{K})$ , which reads

$$H_u(\mathbf{K}) = \begin{pmatrix} \epsilon_{\mathbf{K}} + M_{\mathbf{K}} & Ak_+ \\ Ak_- & \epsilon_{\mathbf{K}} - M_{\mathbf{K}} \end{pmatrix}. \quad (2)$$

The resulting eigenvalues and eigenfunction of Eq. (2) are, respectively,

$$E_{\mathbf{K},l} = \epsilon_{\mathbf{K}} + l[M_{\mathbf{K}}^2 + A^2 k^2]^{1/2} = \epsilon_{\mathbf{K}} + l[\xi_{\mathbf{K},l} + M_{\mathbf{K}}], \quad (3)$$

where  $l = +1$  ( $-1$ ) represents the conduction (valence) band, and

$$\psi_{\mathbf{K},l}(\mathbf{R}) = |\mathbf{K}, l\rangle = a_{\mathbf{K},l} \begin{pmatrix} 1 \\ b_{\mathbf{K},l} \end{pmatrix} e^{i\mathbf{K} \cdot \mathbf{R}}, \quad (4)$$

with  $\mathbf{R} = (x, y, z)$ ,  $\xi_{\mathbf{K},l} = [M_{\mathbf{K}}^2 + A^2 k^2]^{1/2} - lM_{\mathbf{K}}$ ,

$$a_{\mathbf{K},l} = Ak(\xi_{\mathbf{K},l}^2 + A^2 k^2)^{-1/2}, \quad b_{\mathbf{K},l} = l\xi_{\mathbf{K},l}/Ak_-. \quad (5)$$

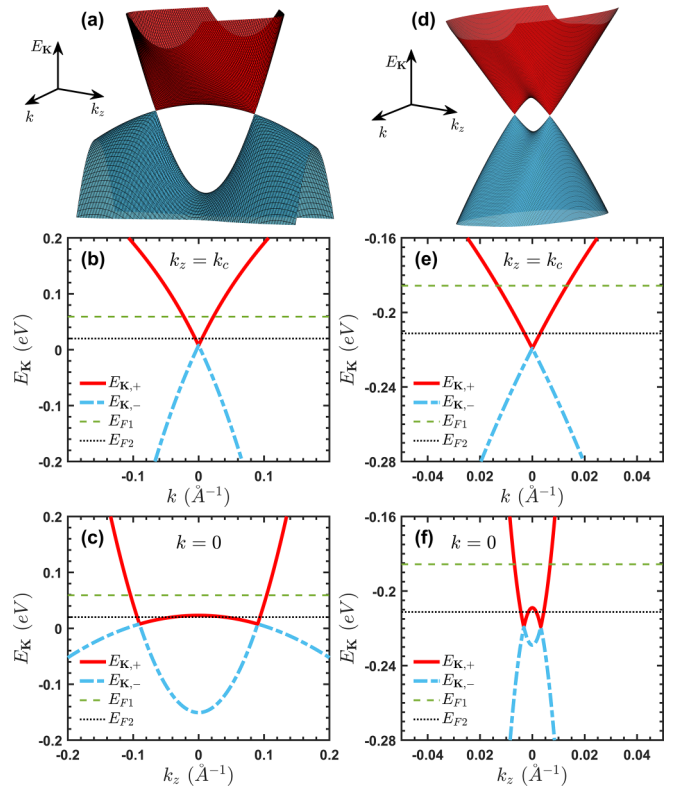


FIG. 1. (a) Energy dispersion  $E_{\mathbf{K}}$  of Na<sub>3</sub>Bi as a function of  $k$  and  $k_z$ , as given by Eq. (3). (b)  $E_{\mathbf{K}}$  as a function of  $k$  at  $k_z = k_c$ . The Dirac point is at  $k = 0$  with energy  $E_0 = 7.6$  meV. (c)  $E_{\mathbf{K}}$  as a function of  $k_z$  at  $k = 0$ . There are two Dirac points at  $k_z = \pm k_c$ . The top of the Berry curvature in the conduction band is  $E_1 \simeq 23$  meV, its bottom in the valence band at  $E_2 \simeq -151$  meV, and they are both located at  $k = 0$  and  $k_z = 0$ . (d)–(f) As in (a)–(c), respectively, for Cd<sub>3</sub>As<sub>2</sub>. The energy of the Dirac point is at  $E_0 \simeq -218.68$  meV. The top of the Berry curvature in the conduction band is  $E_1 \simeq -209$  meV and its bottom in the valence band at  $E_2 \simeq -229$  meV. The red curve shows the conduction band and the blue-dash-dotted curve is the valence band. The green-dashed and black-dotted lines show the Fermi energy  $E_F$  for high- and low-electron densities, respectively, see Figs. 3–6.

Equations (1)–(5) also apply to Cd<sub>3</sub>As<sub>2</sub> but with different parameters [29].

It's worth emphasizing that the band structures of 3D DSMs are different from those of single-layer or multilayer 3D DSMs. In the bulk 3D DSM samples that are unconfined along the  $z$  axis,  $k_z$  is a continuous variable while, in confined systems,  $k_z$  is quantized for sufficiently small thicknesses due to the formed quantum-well structure [2,3]. The finite-size effect removes the band inversion and opens a band gap for sufficiently thin samples [3,31]. The effect weakens with increasing thickness and eventually the band inversion is restored. A recent experimental study confirmed this prediction in Cd<sub>3</sub>As<sub>2</sub> thin films, indicating that this feature is unique and worth exploring further [15]. In our case, the bulk 3D DSMs are extended and, in line with Eqs. (2) and (4), there is no finite-size effect to consider.

In Fig. 1, we show the energy dispersions  $E_{\mathbf{K}}$  of Na<sub>3</sub>Bi (left panels) and of Cd<sub>3</sub>As<sub>2</sub> (right panels) given by Eq. (3). The

first row of panels shows the full dispersions, the second one shows them as functions of  $k$  for fixed  $k_z = k_c$ , and the third as functions of  $k_z$  for  $k = 0$ . We note the following features.

(i) Both Na<sub>3</sub>Bi and Cd<sub>3</sub>As<sub>2</sub> have two symmetric Dirac points at the bottom of the conduction band and the top of the valence band for  $k = 0$  and  $k_z = \pm k_c$ . The corresponding energies are  $E_0 = C_0 + C_1 M_0/M_1$  (Na<sub>3</sub>Bi  $\sim 7.62$  meV, Cd<sub>3</sub>As<sub>2</sub>  $\sim -218.68$  meV).

(ii) Near the two Dirac points, the electron energies are approximately linear, but the dispersions for both bands are asymmetric and depend nonlinearly on  $k$  and  $k_z$ .

(iii) The dispersions along the  $k_z$  direction for both systems show arch-bridge-like Berry curvatures from  $-k_c$  to  $k_c$  in both conduction and valence bands. The top of the arch-bridge-like energy spectrum is reached at  $k = k_z = 0$ , which is in contrast to a conventional 3D electron system where the minimum of the conduction band is at  $k = 0$  and  $k_z = 0$ . The top of the Berry curvature in the conduction band is at  $E_1 = C_0 + |M_0|$  (Na<sub>3</sub>Bi  $\sim 23$  meV, Cd<sub>3</sub>As<sub>2</sub>  $\sim -209$  meV).

(iv) The Berry curvatures in the energy bands imply that the electronic density of states (DOS) should be much smaller for  $E < E_1$  than that for  $E > E_1$  in  $n$ -doped 3D DSMs. Because the effect of Berry curvature in Na<sub>3</sub>Bi is stronger than in Cd<sub>3</sub>As<sub>2</sub>, the DOS in Na<sub>3</sub>Bi should also change more than in Cd<sub>3</sub>As<sub>2</sub>.

(v) The condition of carrier number conservation determines the Fermi energy  $E_F$ . With  $N_e$  the electron density and  $f_+(E_{\mathbf{K},+}) = [e^{(x-E_F^+)/k_B T} + 1]^{-1}$ , the Fermi-Dirac distribution for electrons reads

$$N_e = \frac{1}{\pi^2} \int_0^\infty dk_z \int_0^\infty dk k f_+(E_{\mathbf{K},+}). \quad (6)$$

For  $n$ -doped Na<sub>3</sub>Bi, the Fermi level  $E_F$  is in the conduction band and the Fermi wave vector  $k_F$  along the  $k_z$  axis is much larger than along the  $k$  direction; near the Dirac points it's about 10–20 times larger. But for Cd<sub>3</sub>As<sub>2</sub>  $k_F$  along the  $k$  direction, it is about twice larger than along the  $k_z$  axis. Accordingly, the electronic transitions will be different in Na<sub>3</sub>Bi along the  $k$  or  $k_z$  directions, but in Cd<sub>3</sub>As<sub>2</sub> these differences will be smaller. This conclusion, that Na<sub>3</sub>Bi has stronger anisotropic properties than Cd<sub>3</sub>As<sub>2</sub>, has already been pointed out in the literature [2–6].

(vi) It should be noted that the magnitude of the Fermi velocity  $v_F = 2A$  in Na<sub>3</sub>Bi ( $\simeq 7.473 \times 10^5$  m/s) is similar to that in Cd<sub>3</sub>As<sub>2</sub> ( $\simeq 7.6 \times 10^5$  m/s). This is because the electron effective mass in Cd<sub>3</sub>As<sub>2</sub> [32] ( $\sim 0.02$ – $0.042 m_e$ ), as found experimentally, is much smaller than that in Na<sub>3</sub>Bi [10] ( $\sim 0.11$ – $0.24 m_e$ ). The effective mass term  $M_0 - M_1 k_z^2$  in Eq. (3), with parameters obtained from experiments, leads to similar Fermi velocities in both systems though Na<sub>3</sub>Bi has a larger  $k_F$  wave vector than Cd<sub>3</sub>As<sub>2</sub>.

(vii) As in previous work [11], we measure  $E_F$  from  $E_0 = 7.6$  meV. This suggests that  $E_F$  will locate inside the range of the Berry curvature when the electron density is lower than  $N_e \sim 4 \times 10^{18}$  cm<sup>-3</sup> at low temperatures at which we have  $E_F < E_1 - E_0$  meV [33].

For an  $n$ -type 3D DSM, the valence band is fully occupied and electronic transitions occur from the valence to the conduction band. The density of states (DOS) for the conduction

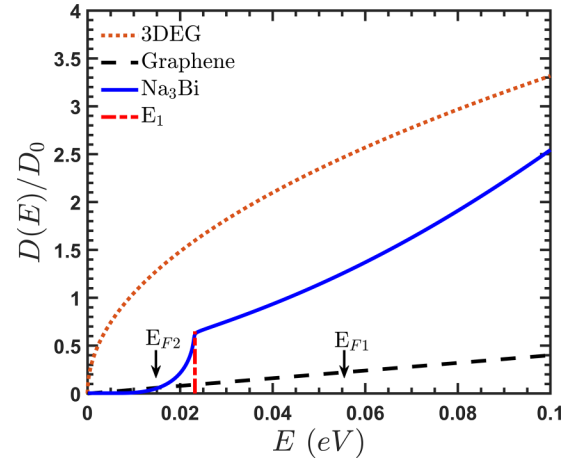


FIG. 2. Density of states (DOS)  $D(E)$  for Na<sub>3</sub>Bi as a function of the electron energy  $E$  (blue curve) with  $D_0 = C_0^2/A^3$  for Na<sub>3</sub>Bi. The top of the Berry curvature in the conduction band is  $E_1 \simeq 23.2$  meV and is marked by the red-dashed curve. At this value of the energy, the velocity  $\partial E_{\mathbf{K}}/\partial k_z$  vanishes (cf. Fig. 1), i.e., it corresponds to an integrable van Hove singularity. The DOS for a 3DEG is shown by the orange-dotted curve using the effective mass  $m^* \simeq 0.11 m_e$  of Na<sub>3</sub>Bi and  $D_0 = m^{*3/2} \sqrt{2|C_0|}/(\pi \hbar^3)$  for a 3DEG. The black-dashed curve is the result for graphene with energy dispersion  $E = \hbar v_F k$  and  $D_0 = C_0^2/(\hbar v_F)^3$ . Arrows indicate the two values of  $E_F$  used to obtain the results shown in Figs. 3–6.

band is given by

$$D_+(E) = -(g_s/\pi) \sum_{k, k_z} \delta(E - E_{\mathbf{K},+}), \quad (7)$$

where  $g_s = 2$  counts for spin degeneracy. Though one of the sums can be evaluated analytically, the result is too cumbersome to be given here. Instead, the  $\delta$  function is replaced by a Lorentzian of width  $\Gamma = 1$  meV, and the integrals over  $k$  and  $k_z$  are carried out numerically.

In Fig. 2, we show the DOS  $D(E)$  as a function of the electron energy  $E$  based on Eq. (7). For clarity, we contrast it with the result for a 3DEG and that for graphene using the details given in the caption. As is known, for a 3DEG the DOS is  $D(E)_{3D} = \sqrt{2} m^{*3} E / (\pi \hbar)^2 \propto E^{1/2}$ . The sharp contrast between the two DOSs implies that a 3DEG has different physical properties than 3D DSMs, especially for  $E < E_1$ , i.e., when  $E_F$  is relatively low and near the Berry curvature. As can be seen, the effect of the Berry curvature is still clear for energies lower than  $E_1 \simeq 23.2$  meV.

These properties of the DOS for 3D DSMs imply that their plasmon modes, for low energies and small momentum, should mainly occur for small  $q_z$ . In addition, it's worth pointing out that the variation of the DOS in Cd<sub>3</sub>As<sub>2</sub> will be different from that of Na<sub>3</sub>Bi although the two systems are similar and have the same energy dispersion. Based on the results of Fig. 1, the electron energy for Cd<sub>3</sub>As<sub>2</sub> along different wave vector directions shows much less difference than in Na<sub>3</sub>Bi, which means that the DOS in Cd<sub>3</sub>As<sub>2</sub> changes less. In addition, the effect of Berry curvature in Cd<sub>3</sub>As<sub>2</sub> will be weaker than in Na<sub>3</sub>Bi and will lead to more weakly anisotropic properties in Cd<sub>3</sub>As<sub>2</sub>; this is in line with the experimental finding in Na<sub>3</sub>Bi [4,5] and Cd<sub>3</sub>As<sub>2</sub> [6,7].

### III. DIELECTRIC FUNCTIONS

As stated in Sec. II, for bulk 3D DSMs the low-energy electronic excitations along  $k$  and  $k_z$  directions are well described by the effective Hamiltonian Eq. (2). Thus, we can study their anisotropic plasmon modes by applying Eqs. (3)–(5) to the RPA dielectric functions based on a 3D Coulomb potential  $V(\mathbf{R})$  with  $\mathbf{R} = (x, y, z)$ .

The electrostatic potential induced by the bare electron-electron ( $e$ - $e$ ) interaction,  $V(\mathbf{R}) = e^2/(\kappa|\mathbf{R}|)$ , can be calculated via [34]

$$\begin{aligned} V_{\text{ind}}(\mathbf{Q}, t) &= V_Q \sum_{\mathbf{K}} \sum_{l, l'} \langle \mathbf{K} + \mathbf{Q}, l' | \delta N | \mathbf{K}, l \rangle \\ &\quad \times \langle \mathbf{K} + \mathbf{Q}, l' | e^{-i\mathbf{Q}\cdot\mathbf{R}} | \mathbf{K}, l \rangle \\ &= \lim_{\eta \rightarrow 0} V_Q V(\mathbf{Q}, t) \sum_{\mathbf{K}} \sum_{l, l'} F_{l', l}(\mathbf{K}, \mathbf{Q}) \Pi_{l', l}(\omega; \mathbf{K}, \mathbf{Q}), \end{aligned} \quad (8)$$

where

$$\Pi_{l', l}(\omega; \mathbf{K}, \mathbf{Q}) = g_s \frac{f_{l'}(E_{\mathbf{K}+\mathbf{Q}, l'}) - f_l(E_{\mathbf{K}, l})}{E_{\mathbf{K}+\mathbf{Q}, l'} - E_{\mathbf{K}, l} - \hbar\omega + i\hbar\eta} \quad (9)$$

is the corresponding density-density correlation function and  $f_l(x) = [e^{(x-E_F^l)/k_B T} + 1]^{-1}$  is the Fermi-Dirac distribution function. Further,  $E_F^l$  is the Fermi energy or chemical potential just above the band  $l$  and  $g_s = 2$  counts for spin degeneracy. Here, the conservation law for momentum flowing into and out of the interaction region has been applied,  $\kappa$  is the dielectric constant for  $\text{Na}_3\text{Bi}$  or  $\text{Cd}_3\text{As}_2$ ,  $\mathbf{Q} = (\mathbf{q}, \varphi, q_z)$  is the change of the electron wave vector during an  $e$ - $e$  scattering event, and  $V_Q = 4\pi e^2/(\kappa Q^2)$  is the 3D Fourier transform of the Coulomb potential induced by the  $e$ - $e$  interaction.  $\delta N$  is the induced density and  $V(\mathbf{Q}, t)$  is the total self-consistent perturbed potential energy.

Using the expressions for the dielectric function  $\hat{\mathcal{E}}(\omega, \mathbf{Q})$ , induced and total potential energy, we obtain

$$\begin{aligned} \hat{\mathcal{E}}(\omega, \mathbf{Q}) &= 1 - \frac{V_{\text{ind}}(\mathbf{Q}, t)}{V(\mathbf{Q}, t)} \\ &= 1 - \lim_{\eta \rightarrow 0} V_Q \sum_{\mathbf{K}} \sum_{l, l'} F_{l', l}(\mathbf{K}, \mathbf{Q}) \Pi_{l', l}(\omega; \mathbf{K}, \mathbf{Q}), \end{aligned} \quad (10)$$

where  $F(\mathbf{K}, \mathbf{Q})$  is the form factor for many-body interactions given by

$$\begin{aligned} F_{l', l}(\mathbf{K}, \mathbf{Q}) &= |\langle \mathbf{K} + \mathbf{Q}, l' | e^{-i\mathbf{Q}\cdot\mathbf{R}} | \mathbf{K}, l \rangle|^2 \\ &= |a_{\mathbf{K}+\mathbf{Q}, l'}^* a_{\mathbf{K}, l} (1 + b_{\mathbf{K}+\mathbf{Q}, l'}^* b_{\mathbf{K}, l})|^2 \\ &= \left| \frac{A^2 k |\mathbf{k} + \mathbf{q}|}{\sqrt{(\xi_{\mathbf{K}+\mathbf{Q}, l'}^2 + A^2 |\mathbf{k} + \mathbf{q}|^2)(\xi_{\mathbf{K}, l}^2 + A^2 k^2)}} \right. \\ &\quad \left. \times \left( 1 + \frac{l l' \xi_{\mathbf{K}, l} \xi_{\mathbf{K}+\mathbf{Q}, l'}}{A^2 [k^2 + (k_x - ik_y)(q_x + iq_y)]} \right) \right|^2, \end{aligned} \quad (11)$$

here,  $|\mathbf{k} + \mathbf{q}|^2 = k^2 + q^2 + 2kq(\cos\theta \cos\varphi + \sin\theta \sin\varphi) = k^2 + q^2 + 2kq \cos(\theta - \varphi)$ ,  $\theta$  is the angle between  $\mathbf{k}$  and the  $x$  axis, and  $\varphi$  is the angle between  $\mathbf{q}$  and the  $x$  axis. Eventually, the dielectric function takes the form

$$\begin{aligned} \hat{\mathcal{E}}(\omega, \mathbf{Q}) &= 1 - \lim_{\eta \rightarrow 0} \frac{4\pi e^2 g_s}{\kappa Q^2} \sum_{\mathbf{K}} \sum_{l, l'} F_{l', l}(\mathbf{K}, \mathbf{Q}) \\ &\quad \times \frac{f_{l'}(E_{\mathbf{K}+\mathbf{Q}, l'}) - f_l(E_{\mathbf{K}, l})}{E_{\mathbf{K}+\mathbf{Q}, l'} - E_{\mathbf{K}, l} - \hbar\omega - i\hbar\eta}. \end{aligned} \quad (12)$$

We now use the identity  $\lim_{\eta \rightarrow 0} [1/(x \pm i\eta)] = \mathcal{P}\{1/x\} \mp i\pi\delta(x)$ , with  $\mathcal{P}\{1/x\}$  the principal value and  $\delta(x)$  the Dirac delta function, to obtain the real and imaginary parts of the dielectric function. Moreover, we replace  $\hbar\eta$  by a small value  $\Gamma$ , assumed to be caused, e.g., by impurity scattering. Then we obtain the real part:

$$\begin{aligned} \mathcal{E}_{\text{Re}}(\omega, \mathbf{Q}) &= 1 - \frac{4\pi e^2 g_s}{\kappa Q^2} \sum_{\mathbf{K}} \sum_{l, l'} F_{l', l}(\mathbf{K}, \mathbf{Q}) \\ &\quad \times [f_{l'}(E_{\mathbf{K}+\mathbf{Q}, l'}) - f_l(E_{\mathbf{K}, l})] \\ &\quad \times \frac{(E_{\mathbf{K}+\mathbf{Q}, l'} - E_{\mathbf{K}, l} - \hbar\omega)}{(E_{\mathbf{K}+\mathbf{Q}, l'} - E_{\mathbf{K}, l} - \hbar\omega)^2 + \Gamma^2}. \end{aligned} \quad (13)$$

Meanwhile, the imaginary part  $\mathcal{E}_{\text{Im}}(\omega, \mathbf{Q})$  becomes

$$\begin{aligned} \mathcal{E}_{\text{Im}}(\omega, \mathbf{Q}) &= \frac{4\pi^2 e^2 g_s}{\kappa Q^2} \sum_{\mathbf{K}} \sum_{l, l'} F_{l', l}(\mathbf{K}, \mathbf{Q}) [f_{l'}(E_{\mathbf{K}+\mathbf{Q}, l'}) \\ &\quad - f_l(E_{\mathbf{K}, l})] \delta(E_{\mathbf{K}+\mathbf{Q}, l'} - E_{\mathbf{K}, l} - \hbar\omega). \end{aligned} \quad (14)$$

It is very difficult to study the plasmon mode along an arbitrary direction of the 3D wave vector  $\mathbf{Q}$ . Instead, we decompose it in two components:  $\mathbf{Q}_{\perp} = (0, 0, q_z)$  perpendicular to the  $(x, y)$  plane, which will only act along the  $k_z$  direction, and  $\mathbf{Q}_{\parallel} = (q, \varphi, 0)$ , with  $\varphi$  the angle between  $\mathbf{q}$  and  $x$  axis, which is parallel to this plane.

#### A. $\mathbf{Q}$ perpendicular to the $(x, y)$ plane

In the first case, the real part of  $\hat{\mathcal{E}}(\mathbf{K}, \mathbf{Q})$  from Eq. (13) for  $\mathbf{Q}_{\perp} = (0, 0, q_z)$  becomes

$$\begin{aligned} \mathcal{E}_{\text{Re}}^{\perp}(\omega, q_z) &= 1 - \frac{8e^2}{\kappa\pi q_z^2} \sum_{l, l'} \int_0^{\infty} dk_z \int_0^{\infty} dk \\ &\quad \times F_{l', l}(\mathbf{K}, q_z) [f_{l'}(E_{\mathbf{K}, q_z, l'}) - f_l(E_{\mathbf{K}, l})] \\ &\quad \times \frac{(E_{\mathbf{K}, q_z, l'} - E_{\mathbf{K}, l} - \hbar\omega)}{(E_{\mathbf{K}, q_z, l'} - E_{\mathbf{K}, l} - \hbar\omega)^2 + \Gamma^2}, \end{aligned} \quad (15)$$

with

$$E_{\mathbf{K}, q_z, l'} = C_0 + C_1(k_z + q_z)^2 + C_2 k^2 + l' \sqrt{M_{q_z}^2 + A^2 k^2}, \quad (16)$$

$$\begin{aligned} M_{q_z} &= [M_0 - M_1(k_z + q_z)^2 - M_2 k^2], \\ F_{l', l}(\mathbf{K}, q_z) &= \left| \frac{A^2 k^2}{\sqrt{(\xi_{\mathbf{K}, q_z, l'}^2 + A^2 k^2)(\xi_{\mathbf{K}, l}^2 + A^2 k^2)}} \right. \\ &\quad \left. \times \left( 1 + \frac{l l' \xi_{\mathbf{K}, l} \xi_{\mathbf{K}, q_z, l'}}{A^2 k^2} \right) \right|^2, \end{aligned} \quad (17)$$



where

$$\xi_{\mathbf{K},q_z,l'} = \sqrt{M_q^2 + A^2 k^2} - l' M_{q_z}. \quad (18)$$

In the meantime, assuming a broadening of the energy levels due to scattering, we can write  $\delta(E) \approx (\Gamma/\pi)(E^2 + \Gamma^2)^{-1}$  in Eq. (14), where  $\Gamma = \hbar/\tau$  and  $\tau$  is the lifetime. Then the imaginary part of  $\hat{\mathcal{E}}(\mathbf{K}, \mathbf{Q})$  for  $\mathbf{Q}_\perp = (0, 0, q_z)$  becomes

$$\begin{aligned} \mathcal{E}_{\text{Im}}^\perp(\omega, q_z) &= \frac{8e^2 \hbar}{\kappa \pi \tau q_z^2} \sum_{l',l} \int_0^\infty dk_z \int_0^\infty dk k \\ &\times F_{l',l}(\mathbf{K}, q_z) [f_{l'}(E_{\mathbf{K},q_z,l'}) - f_l(E_{\mathbf{K},l})] \\ &\times [\Gamma^2 + (E_{\mathbf{K},q_z,l'} - E_{\mathbf{K},l} - \hbar\omega)^2]^{-1}. \end{aligned} \quad (19)$$

### B. Q parallel to the (x, y) plane

In this case, we take the wave vector  $\mathbf{Q}$  as  $\mathbf{Q}_\parallel = (q, \varphi, 0)$ , where  $\varphi$  is the angle between  $\mathbf{q}$  and the  $x$  axis. From Eq. (13), we obtain the real part of  $\hat{\mathcal{E}}(\mathbf{K}, \mathbf{Q})$  as

$$\begin{aligned} \mathcal{E}_{\text{Re}}^\parallel(\omega, \mathbf{q}, \varphi) &= 1 - \frac{4e^2}{\kappa \pi^2 q^2} \sum_{l',l} \int_0^\infty dk_z \int_0^{2\pi-\varphi} d\phi \int_0^\infty dk k \\ &\times F_{l',l}(\mathbf{K}, \mathbf{q}, \varphi) [f_{l'}(E_{\mathbf{K},\mathbf{q},\varphi}) - f_l(E_{\mathbf{K}})] \\ &\times \frac{E_{\mathbf{K},\mathbf{q},\varphi} - E_{\mathbf{K}} - \hbar\omega}{(E_{\mathbf{K},\mathbf{q},\varphi} - E_{\mathbf{K}} - \hbar\omega)^2 + \Gamma^2}, \end{aligned} \quad (20)$$

with

$$E_{\mathbf{K},\mathbf{q},\varphi} = C_0 + C_1 k_z^2 + C_2 |\mathbf{k} + \mathbf{q}|^2 + l' \sqrt{M_q^2 + A^2 |\mathbf{k} + \mathbf{q}|^2}, \quad (21)$$

where  $M_q = M_0 - M_1 k_z^2 - M_2 |\mathbf{k} + \mathbf{q}|^2$ ,

$$\begin{aligned} F_{l',l}(\mathbf{K}, \mathbf{q}, \varphi) &= \left| \frac{A^2 k |\mathbf{k} + \mathbf{q}|}{\sqrt{(\xi_{\mathbf{K},\mathbf{q},\varphi,l'}^2 + A^2 |\mathbf{k} + \mathbf{q}|^2)(\xi_{\mathbf{K},l}^2 + A^2 k^2)}} \right. \\ &\left. \times (1 + ll' \xi_{\mathbf{K},l} \xi_{\mathbf{K},\mathbf{q},\varphi,l'} / A^2 k |\mathbf{k} + \mathbf{q}|) \right|^2, \end{aligned} \quad (22)$$

and

$$\xi_{\mathbf{K},\mathbf{q},\varphi,l'} = \sqrt{M_q^2 + A^2 |\mathbf{k} + \mathbf{q}|^2} - l' M_q. \quad (23)$$

By applying relaxation time approximation to Eq. (14), the imaginary part of  $\hat{\mathcal{E}}(\mathbf{K}, \mathbf{Q})$  for  $\mathbf{Q}_\parallel = (\mathbf{q}, \varphi, 0)$  has the form

$$\begin{aligned} \mathcal{E}_{\text{Im}}^\parallel(\omega, \mathbf{q}, \varphi) &= \frac{4e^2 \hbar}{\kappa \pi^2 \tau q^2} \sum_{l',l} \int_0^\infty dk_z \int_0^{2\pi-\varphi} d\phi \int_0^\infty dk k \\ &\times F_{l',l}(\mathbf{K}, \mathbf{q}, \varphi) [f_{l'}(E_{\mathbf{K},\mathbf{q},\varphi}) - f_l(E_{\mathbf{K}})] \\ &\times [\Gamma^2 + (E_{\mathbf{K},\mathbf{q},\varphi,l'} - E_{\mathbf{K},l} - \hbar\omega)^2]^{-1}. \end{aligned} \quad (24)$$

Here, we made the change  $\phi = \theta - \varphi$ , so  $|\mathbf{k} + \mathbf{q}|^2 = k^2 + q^2 + 2kq \cos(\theta - \varphi)$ . Then the integration over  $\theta$  from 0 to  $2\pi$  becomes one over  $\phi$  from 0 to  $(2\pi - \varphi)$ , which describes how different wave vector  $\mathbf{q}$  directions affect the dielectric function. After obtaining the expressions of the dielectric function for 3D DSMs in different directions, we consider the transitions between different energy bands. The band index

TABLE I. The energy band parameters and dielectric constant of  $\text{Na}_3\text{Bi}$  are taken from Refs. [2,37], respectively. Note that for  $\text{Cd}_3\text{As}_2$ , the original band parameters are  $M'_0 = -0.060$  eV,  $M'_1 = 96$  eV $\text{\AA}^2$ , and  $M_3 = 0.05$  eV. For small momenta  $|k_z| \ll M_3/\sqrt{M'_1}$ , the energy dispersion in  $\text{Cd}_3\text{As}_2$  will have the same form as in  $\text{Na}_3\text{Bi}$ , and the band parameters become  $M_0 = M'_0 + |M_3|$  and  $M_1 = 0.5M'_1/|M_3|$  in Eqs. (1)–(4) [29]. The dielectric constant for  $\text{Cd}_3\text{As}_2$  is taken from Ref. [24].

Na <sub>3</sub> Bi band parameters			
$C_0$ (eV)	$C_1$ (eV $\text{\AA}^2$ )	$C_2$ (eV $\text{\AA}^2$ )	$M_0$ (eV)
-0.06382	8.7536	-8.4008	-0.8686
$M_1$ (eV $\text{\AA}^2$ )	$M_2$ (eV $\text{\AA}^2$ )	$A$ (eV $\text{\AA}$ )	$\kappa$
-10.6424	-10.361	2.4598	5.99
Cd <sub>3</sub> As <sub>2</sub> band parameters			
$C_0$ (eV)	$C_1$ (eV $\text{\AA}^2$ )	$C_2$ (eV $\text{\AA}^2$ )	$M_0$ (eV)
-0.219	-30	-16	-0.01
$M_1$ (eV $\text{\AA}^2$ )	$M_2$ (eV $\text{\AA}^2$ )	$A$ (eV $\text{\AA}$ )	$\kappa$
960	18	2.75	12

$l = 1$  ( $-1$ ) represents the conduction (valence) band, and the dielectric function will have four parts:

$$\sum_{ll'} \hat{\mathcal{E}} = \mathcal{E}_{++} + \mathcal{E}_{-+} + \mathcal{E}_{+-} + \mathcal{E}_{--}. \quad (25)$$

Since we focus on  $n$ -type 3D DSMs, in which the conduction band is occupied, the valence band is fully occupied so  $f_-(x) = 1$ , and  $\Pi_{l',l}(\omega; \mathbf{K}, \mathbf{Q}) = 0$  for  $l' = l = -1$ . At the same time, electron transitions from the conduction band ( $l = +1$ ) to the valence band ( $l' = -1$ ) have only a very small influence on plasmon modes, so we take  $\mathcal{E}_{+-} \simeq 0$ . Thus, eventually we consider only intraband transitions in the conduction band ( $\mathcal{E}_{++}$ ) and interband transitions from the valence to the conduction band ( $\mathcal{E}_{-+}$ ) into account. Then, the resulting plasmon modes are the solutions of  $\text{Re}[\hat{\mathcal{E}}(\omega, \mathbf{Q})] = |\mathcal{E}_{\text{Re}}(\omega, \mathbf{Q})| = 0$ . The energy loss rate can be evaluated using the imaginary part of the dielectric function through the energy loss function:

$$E_{\text{loss}} = -\text{Im} \left[ \frac{1}{\hat{\mathcal{E}}(\omega, \mathbf{Q})} \right] = \frac{-\mathcal{E}_{\text{Im}}(\omega, \mathbf{Q})}{\mathcal{E}_{\text{Re}}(\omega, \mathbf{Q})^2 - \mathcal{E}_{\text{Im}}(\omega, \mathbf{Q})^2}. \quad (26)$$

As shown in Fig. 1, 3D DSMs have anisotropic energy dispersions, but in the  $(x, y)$  plane their dispersions are isotropic and similar to that of graphene. Thus, we first consider the simple case in which  $\mathbf{q}$  is parallel to  $\mathbf{k}$  by setting  $\varphi = 0$  in Eqs. (20) and (24). Following the standard procedure [35], we first obtain the plasmon dispersion from the zeros of the real part of the dielectric function and then calculate the energy loss using Eq. (26).

## IV. RESULTS AND DISCUSSION

For the numerical calculations, we use the band parameters for  $\text{Na}_3\text{Bi}$  shown in Table I [2]. They were determined by fitting the energy spectrum of the effective Hamiltonian in Eq. (1) to those obtained from *ab initio* calculations and the ARPES experimental results [4,5] since both agree well with those of Ref. [2]. For the 3D DSM  $\text{Cd}_3\text{As}_2$ , the experimental works from ARPES measurements [6,7] and scanning

microscopy measurements [29] indicate that the energy spectrum deduced from experiments is basically the same as the theoretical one [3], though with some minor differences. The main one is that the experimentally determined Fermi velocities in  $\text{Cd}_3\text{As}_2$  [6,29] are much larger than the theoretical ones [3]. As a result, we use the band parameters from the ARPES measurements shown in Table I [29]. Furthermore, it has been shown experimentally that for 3D DSMs, the lifetime is different for samples with different carrier densities, but for low temperatures both  $\text{Na}_3\text{Bi}$  and  $\text{Cd}_3\text{As}_2$  samples exhibit fast lifetimes ( $\sim 1-7$  ps) [10,16,36]. Hence, we use 6.71 ps for  $\text{Na}_3\text{Bi}$  [10] and 6.87 ps for  $\text{Cd}_3\text{As}_2$  [36].

As shown in Fig. 2, the DOS for 3DEG, graphene, and 3D DSMs are different from each other. Accordingly, their plasmon modes will also be different. In the long-wavelength limit ( $\mathbf{Q} \rightarrow 0$ ), the plasmon dispersion of 3DEG is given by an optical-like formula  $\omega_Q = \omega_p + 3v_F^2 Q^2 / (10\omega_p) \sim Q^2$ , where  $\omega_p = [N_e e^2 / (m\kappa_0)]^{1/2}$  is the plasma frequency,  $\kappa_0$  the vacuum dielectric constant, and  $v_F = \hbar k_F / m$  is the Fermi velocity. In a real metal, e.g., sodium, we have  $N_e \sim 10^{23} \text{ cm}^{-3}$ , the plasmon energy  $\hbar\omega_p \sim 5.9 \text{ eV}$  is much larger than  $k_B T \sim 25 \text{ meV}$ , so plasmons in a 3DEG are not easily, i.e., thermally excitable; this means it's very difficult to directly observe them in experiments. However, for graphene in the long-wavelength limit ( $\mathbf{q} \rightarrow 0$ ), the dispersion relation  $\omega_q = (2e^2 E_F q / \kappa_0)^{1/2} \sim q^{1/2} \sim N_e^{1/4}$  with  $E_F = \hbar v_F k_F$ ,  $k_F = (\pi N_e)^{1/2}$ , is acousticlike and depends strongly on  $q$  [38]. In addition, a conventional 2D electron gas (2DEG) has a dispersion relation similar to graphene  $\omega_q \sim q^{1/2} \sim N_e^{1/2}$  [39]. The plasmon energies for both 2DEG and graphene are  $\hbar\omega_q \rightarrow 0$  for  $q \rightarrow 0$ , i.e., quite small. Consequently, plasmons in them are easier to excite and observe in experiments.

Figure 3 shows the plasmon dispersion and energy loss rate for different wave vector directions for high electron density in  $\text{Na}_3\text{Bi}$  and fixed temperature. The corresponding Fermi level is much higher than the Berry curvature [cf. green-dashed line in Figs. 1(b) and 1(c)], and the Fermi wave vector  $k_{Fz}$  is about five times larger than  $k_F$ .

We notice the following

(i) Figures 3(a) and 3(b) show the dispersion relations along  $q$  and  $q_z$  are anisotropic in  $\text{Na}_3\text{Bi}$ . This is in line with the anisotropic band structure of  $\text{Na}_3\text{Bi}$  shown in Figs. 1(b) and 1(c), which indicates that its electron excitation energy  $E_{\mathbf{k}}$  requires a different momentum  $k$  or  $k_z$  along different directions.

(ii) The plasmon energy  $\hbar\omega \rightarrow 0$ , in the long-wavelength limit  $q \rightarrow 0$  and  $q_z \rightarrow 0$ , which is in sharp contrast with the results for a 3DEG and also with those for 3D DSMs with a single Dirac point [24–26]. The collective oscillations of electrons should be easier to excite and observe in  $\text{Na}_3\text{Bi}$  due to its unique energy band.

(iii) The dispersions are linear for small  $q$  or  $q_z$  ( $\hbar\omega \propto q$ ,  $q_z$ ), but with increasing  $q$  or  $q_z$  they become similar to that of a 3DEG ( $\hbar\omega \propto q^2$  or  $q_z^2$ ). Also, these changes are more distinct vs  $q_z$  in Figs. 3(b) and 3(d) than vs  $q$  in Figs. 3(a) and 3(c). In Fig. 1(b), we found that the electron energy along the  $k$  direction is approximately linear in  $k$  in a higher energy range, but along the  $k_z$  direction, cf. Fig. 1(c), it is linear only close to the Dirac points whereas at high energies it becomes

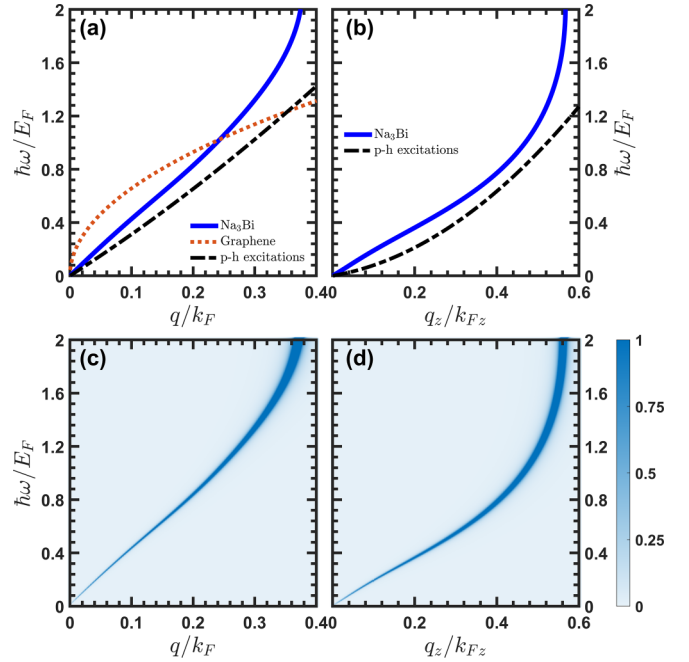


FIG. 3. Dispersion relations and energy loss functions in  $\text{Na}_3\text{Bi}$  along different  $\mathbf{Q}$  directions at temperature  $T = 10 \text{ K}$ , electron density  $N_e = 1 \times 10^{19} \text{ cm}^{-3}$  [see green-dashed lines in Figs. 1(b) and 1(c)], corresponding to  $E_{F1} \simeq 59.076 \text{ meV}$ , and lifetime  $\tau = 6.71 \text{ ps}$ . In (a) and (c), we have  $\mathbf{Q}_{\parallel} = (q, \varphi, 0)$  at  $\varphi = 0$ ; the Fermi wave vector  $k_F$  along the  $k$  direction is about  $\sim 2.25 \times 10^8 \text{ m}^{-1}$ . In (b) and (d), we have  $\mathbf{Q}_{\perp} = (0, 0, q_z)$ ; the Fermi wave vector  $k_{Fz}$  along the  $k_z$  direction is about  $\sim 10.4 \times 10^8 \text{ m}^{-1}$ . The orange-dotted curve in (a) is graphene's plasmon dispersion relation for  $N_e = 1 \times 10^{12} \text{ cm}^{-2}$ . The black-dash-dotted curves in (a) and (b) represent, for a 3DEG with  $m^* \simeq 0.24m_e$ , the beginning of the particle-hole (p-h) excitations area in which  $\omega \simeq \hbar^2(q^2 + 2qk_F)/2m^*$ .

parabolic. That is, the plasmon dispersion vs  $q$  is linear in a broader range than vs  $q_z$ .

(iv) The energy loss function, corresponding to Fig. 3 panels (a) and (b), is shown in Fig. 3 panels (c) and (d), respectively. As expected, plasmons appear as peaks in the energy loss functions for both  $\mathbf{Q}_{\parallel}$  and  $\mathbf{Q}_{\perp}$ . Meanwhile, the wave-vector dependence is consistent with that of the plasmon dispersion and it is anisotropic. The energy loss peaks are broader at large  $q$  and  $q_z$ , but still they converge up to a high energy  $\hbar\omega = 2E_F$ .

(v) The plasmon energies will involve the particle-hole (p-h) excitation continuum in 3DEG, graphene [39], and single-cone 3D DSMs [25,26], e.g., for  $\hbar\omega < \hbar^2(Q_c^2 + 2Q_c K_F)/(2m^*)$  and  $Q > Q_c$  in 3DEG. However, we found that in  $\text{Na}_3\text{Bi}$  the plasmon dispersion curves only occur in a relatively small wave vector range and the plasmon energies are above the continuum of the 3D p-h excitations in the entire wave vector range in both Figs. 3(a) and 3(b). Meanwhile, we would like to point out that this paper is based on the effective Hamiltonian, which is only valid for small momenta and low-energy ranges. Thus, our paper indicates that plasmons in  $\text{Na}_3\text{Bi}$  do not merge into the Landau damping range, i.e., the plasmon energy will not decay by single-particle excitations for small  $q$  and  $q_z$ .

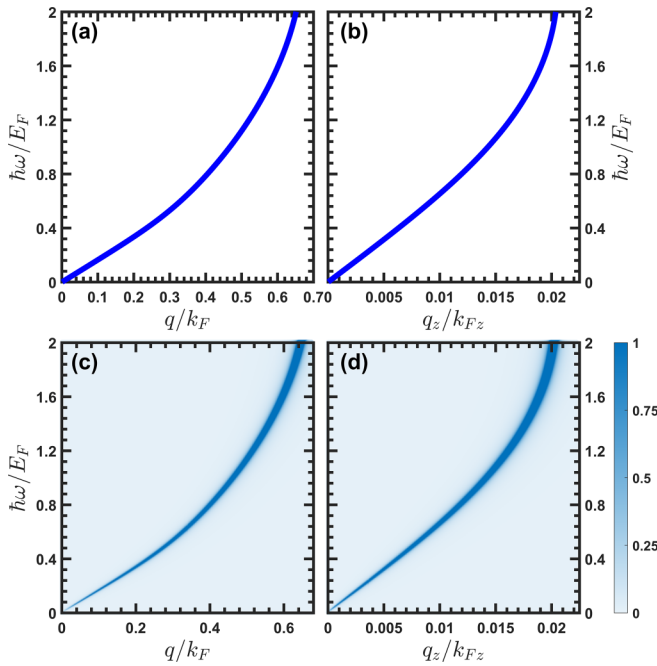


FIG. 4. As in Fig. 3 with electron density  $N_e = 1 \times 10^{17} \text{ cm}^{-3}$  [see black-dotted lines in Figs. 1(b) and 1(c), corresponding to  $E_{F2} \simeq 14.634 \text{ meV}$ ]. For  $\mathbf{Q}_{\parallel} = (q, \varphi, 0)$  at  $\varphi = 0$ , the Fermi wave vector  $k_F$  along the  $k$  direction is about  $\sim 0.298 \times 10^8 \text{ m}^{-1}$ . For  $\mathbf{Q}_{\perp} = (0, 0, q_z)$ , the Fermi wave vector  $k_{Fz}$  along the  $k_z$  axis is about  $\sim 9.24 \times 10^8 \text{ m}^{-1}$ .

The results of Fig. 3 are for high values of the electron density  $N_e = 1 \times 10^{19} \text{ cm}^{-3}$  and  $E_F$  is much higher than the energy for Berry curvature region, cf. green-dashed line in Fig. 1(b). A significant change occurs for low electron density,  $N_e = 1 \times 10^{17} \text{ cm}^{-3}$ , and  $E_F$  is lower than the Berry curvature, cf. black-dotted line in Fig. 1(b). The results are shown in Fig. 4. Although the overall trend looks similar, the range of the relevant wave vectors changes. In particular, that for  $q_z$  shrinks dramatically, it's approximately 30 times shorter whereas  $q$  is only about four times shorter. This is due to the presence of the Berry curvature in energy bands. As seen from Fig. 2, the DOS of  $\text{Na}_3\text{Bi}$  decreases rapidly with decreasing  $E_F$ , especially for  $E_F < E_1$ , and Fig. 1 indicates that the Berry curvature mainly effects the energy along  $k_z$  direction. As a result, reducing electron doping leads to a much smaller wave vector dependence of plasmon dispersion for  $\mathbf{Q}_{\perp}$ . Similar effects of the Berry curvature were reported in Ref. [11].

The results shown in Figs. 3 and 4 are for  $\text{Na}_3\text{Bi}$ . The corresponding ones for  $\text{Cd}_3\text{As}_2$  are shown in Figs. 5 and 6, respectively. As shown, the plasmon dispersion relations and energy losses for high electron density  $\text{Cd}_3\text{As}_2$  are similar to those in  $\text{Na}_3\text{Bi}$ . In some detail, we observe the following:

- (i) The plasmon energies are  $\hbar\omega \rightarrow 0$  for  $q \rightarrow 0$  and  $q_z \rightarrow 0$ .
- (ii) The plasmon modes are anisotropic, the plasmon dispersions are linear for small  $q$  and  $q_z$  but become parabolic with increasing  $q$  and  $q_z$ . The dispersion for  $q$  is linear in a boarder range than  $q_z$ .

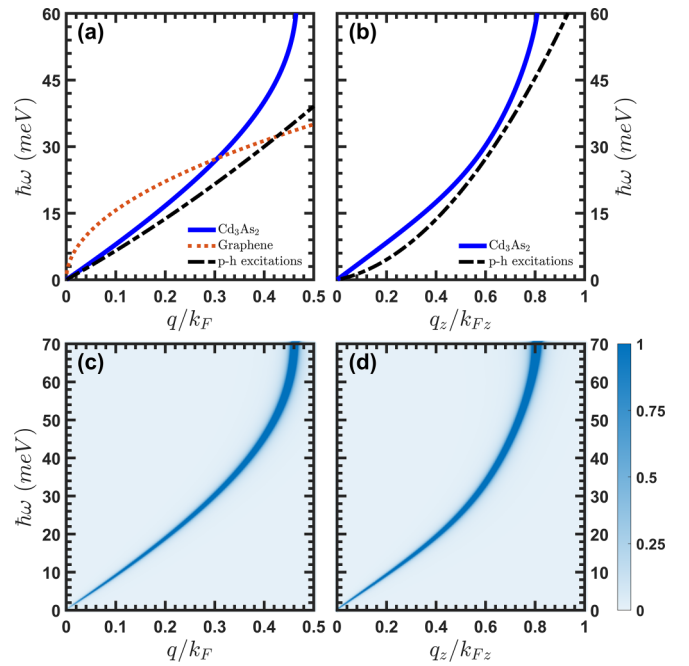


FIG. 5. Plasmon dispersions and energy loss functions in  $\text{Cd}_3\text{As}_2$  along different  $\mathbf{Q}$  directions at fixed temperature  $T = 10 \text{ K}$ , electron density  $N_e = 1 \times 10^{19} \text{ cm}^{-3}$  [see Figs. 1(e) and 1(f), corresponding to  $E_{F1} \simeq -185.651 \text{ meV}$ ], and lifetime  $\tau = 6.87 \text{ ps}$ . For  $\mathbf{Q}_{\parallel} = (q, \varphi, 0)$  at  $\varphi = 0$ , the Fermi wave vector  $k_F$  along the  $k$  direction is about  $\sim 1.33 \times 10^8 \text{ m}^{-1}$ . For  $\mathbf{Q}_{\perp} = (0, 0, q_z)$ , the Fermi wave vector  $k_{Fz}$  along the  $k_z$  axis is about  $\sim 0.68 \times 10^8 \text{ m}^{-1}$ . The orange-dotted curve in (a) is graphene's dispersion relation for  $N_e = 1 \times 10^{12} \text{ cm}^{-2}$ . The black-dash-dotted curves in (a) and (b) represent, for a 3DEG with  $m^* \simeq 0.24m_e$ , the beginning of the particle-hole (p-h) excitations area in which  $\omega \simeq \hbar^2(q^2 + 2qk_F)/2m^*$ .

(iii) The plasmon energies in both directions do not involve p-h excitations, so its plasma oscillations will also not be damped nor will they decay into the single-particle continuum. For low electron densities, cf. Fig. 6, a significant small  $q_z$  dependence for plasmon energy can be found and results from the Berry curvature of the energy band.

The overall trend is similar to  $\text{Na}_3\text{Bi}$ , but we notice some differences between  $\text{Na}_3\text{Bi}$  and  $\text{Cd}_3\text{As}_2$ . We mentioned that  $\text{Cd}_3\text{As}_2$  has less anisotropic properties than  $\text{Na}_3\text{Bi}$  in Figs. 1 and 2. Specifically, when we reduce the electron doping, both plasmon wave vectors for  $\text{Na}_3\text{Bi}$  and  $\text{Cd}_3\text{As}_2$  will decrease, but the  $q_z$  range in  $\text{Na}_3\text{Bi}$  will shrink much more than that in  $\text{Cd}_3\text{As}_2$ . In addition, the  $k_{Fz}$  value in  $\text{Cd}_3\text{As}_2$  is smaller than its  $k_F$  whereas in  $\text{Na}_3\text{Bi}$   $k_{Fz}$  is about 20 times larger than its  $k_F$ . We emphasize that in both 3D DSMs the distance of  $E_F$  from the Berry curvature importantly affects the pertinent wave vector ranges.

Finally, it is of interest to see how the results vs  $q$  change when  $q_z$  is not zero and how the results change vs  $q_z$  when  $q$  takes certain values. We show them in Figs. 7(a) and 7(b) for  $\text{Na}_3\text{Bi}$  and for  $\text{Cd}_3\text{As}_2$  in Figs. 7(c) and 7(d), using the parameters of the caption and the constant  $q_z$  or  $q$  values specified in the insets. As shown in Fig. 7, for  $q_z \neq 0$  (or  $q \neq 0$ ), the dispersion becomes similar to that of a 3DEG as

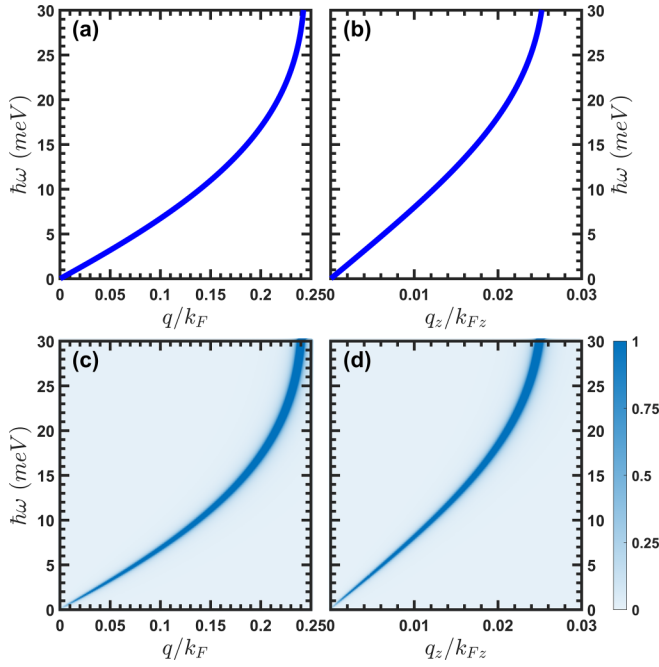


FIG. 6. As in Fig. 5 with electron density  $N_e = 1 \times 10^{17} \text{ cm}^{-3}$  [see Figs. 1(e) and 1(f), corresponding to  $E_{F2} \simeq -211.237 \text{ meV}$ ]. For  $\mathbf{Q}_{\parallel} = (\mathbf{q}, \varphi, 0)$  at  $\varphi = 0$ , the Fermi wave vector  $k_F$  along the  $k$  direction is about  $\sim 0.301 \times 10^8 \text{ m}^{-1}$ . For  $\mathbf{Q}_{\perp} = (0, 0, q_z)$ , the Fermi wave-vector  $k_{Fz}$  along the  $k_z$  axis is about  $\sim 0.438 \times 10^8 \text{ m}^{-1}$ .

either  $q_z$  or  $q$  take some constant values and the anisotropic features are distinct.

Considering the results from all figures, we see that the plasmon modes in the bulk materials  $\text{Na}_3\text{Bi}$  and  $\text{Cd}_3\text{As}_2$  show unique properties and advantages over other materials. For instance, 3D DSMs have similar gapless Dirac properties as graphene, such as high carrier mobility, but the samples for bulk 3D DSMs are easier to manufacture. Also, in 3D DSMs the plasmons are easier to observe than in metals due to their energy  $\hbar\omega$  being close to  $k_B T \sim 25 \text{ meV}$  as we discussed before. The Fermi energy  $E_F$  related to the carrier density is gate tunable in 3D DSMs [12]; therefore, the plasmons, which are sensitively affected by the position of  $E_F$  relative to the Berry curvature region of the bands, will also have the anisotropic gate-tunable properties in sharp contrast to other 3D materials such as multilayered graphene [27], Weyl semimetals [28], and isotropic Dirac semimetals [26]. Furthermore, other interesting properties, such as anisotropic plasmon polaritons and surface plasmons can be expected based on our results.

## V. SUMMARY

We presented a premiere RPA treatment of collective excitations in 3D DSMs  $\text{Na}_3\text{Bi}$  and  $\text{Cd}_3\text{As}_2$  using one-electron properties derived from a  $\mathbf{k} \cdot \mathbf{p}$  Hamiltonian. The density of states of these DSMs differ significantly from those of a 3D electron gas or graphene. The anisotropy of the

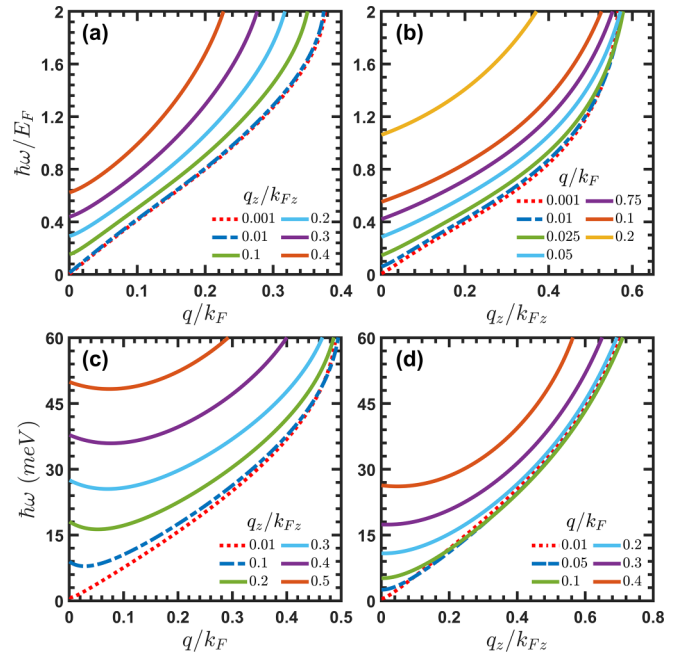


FIG. 7. (a) Plasmon dispersion for  $\text{Na}_3\text{Bi}$  as a function of  $q$  at fixed temperature  $T = 10 \text{ K}$ , electron density  $N_e = 1 \times 10^{19} \text{ cm}^{-3}$ , lifetime  $\tau = 6.71 \text{ ps}$ , and fixed  $q_z$ . (b) Plasmon dispersion for  $\text{Na}_3\text{Bi}$  with  $q$  and  $q_z$  interchanged is shown. (c), (d) As in (a) and (b), respectively, for  $\text{Cd}_3\text{As}_2$ , for the same temperature and electron density, and  $\tau = 6.87 \text{ ps}$ . All curves for selected  $q_z$  or  $q$  isovalues are marked as shown in the insets.

one-electron spectrum shows up in the dispersion relations that are markedly different from those of graphene or a 3D electron gas. The same holds for the energy-loss function. There are important differences between results valid for high and low electron densities that result in the Fermi energy being far or close to the region of the Berry curvature of the bands. One particularly worth mentioning is that for  $E_F$  less than the energy at which  $v_z$  vanishes, the range of the relevant wave vectors  $q$  and  $q_z$  shrinks, especially the one for  $q_z$  shrinks by nearly a factor of 10. Therefore, changing the electron density of 3D DSMs allows one to tune the frequency range of their plasmon modes, particularly along the  $z$  direction. Moreover, other intriguing properties like anisotropic plasmon polaritons and surface plasmons, which will also be affected by electron density due to the Berry curvature of the energy band, can be expected.

## ACKNOWLEDGMENTS

Q.N.L. acknowledges financial support from China Scholarship Council (Grant No. 202207030017). This work was also supported by the National Natural Science foundation of China (Grants No. U2230122, No. U2067207, and No. 12364009), the Research Foundation Flanders (FWO-VI), and Shenzhen Science and Technology Program (Grant No. KQTD20190929173954826).



- [1] S. M. Young, S. Zaheer, J. C. Y. Teo, C. L. Kane, E. J. Mele, and A. M. Rappe, *Phys. Rev. Lett.* **108**, 140405 (2012).
- [2] Z. J. Wang, Y. Sun, X.-Q. Chen, C. Franchini, G. Xu, H. M. Weng, X. Dai, and Z. Fang, *Phys. Rev. B* **85**, 195320 (2012).
- [3] Z. J. Wang, H. M. Weng, Q. S. Wu, X. Dai, and Z. Fang, *Phys. Rev. B* **88**, 125427 (2013).
- [4] S.-Y. Xu, C. Liu, S. K. Kushwaha, R. Sankar, J. W. Krizan, I. Belopolski, M. Neupane, G. Bian, N. Alidoust, T.-R. Chang, H.-T. Jeng, C.-Y. Huang, W.-F. Tsai, H. Lin, P. P. Shibayev, F.-C. Chou, R. J. Cava, and M. Z. Hasan, *Science* **347**, 294 (2015).
- [5] Z. K. Liu, B. Zhou, Y. Zhang, Z. J. Wang, H. M. Weng, D. Prabhakaran, S.-K. Mo, Z. X. Shen, Z. Fang, X. Dai, Z. Hussain, and Y. L. Chen, *Science* **343**, 864 (2014).
- [6] M. Neupane, S.-Y. Xu, R. Sankar, N. Alidoust, G. Bian, C. Liu, I. Belopolski, T.-R. Chang, H.-T. Jeng, H. Lin, A. Bansil, F. C. Chou, and M. Z. Hasan, *Nat. Commun.* **5**, 3786 (2014).
- [7] Z. K. Liu, J. Jiang, B. Zhou, Z. J. Wang, Y. Zhang, H. M. Weng, D. Prabhakaran, S.-K. Mo, H. Peng, P. Dudin, T. Kim, M. Hoesch, Z. Fang, X. Dai, Z. X. Shen, D. L. Feng, Z. Hussain, and Y. L. Chen, *Nat. Mater.* **13**, 677 (2014).
- [8] S. Borisenko, Q. Gibson, D. Evtushinsky, V. Zabolotnyy, B. Büchner, and R. J. Cava, *Phys. Rev. Lett.* **113**, 027603 (2014).
- [9] T. Liang, Q. Gibson, M. N. Ali, M. Liu, R. J. Cava, and N. P. Ong, *Nat. Mater.* **14**, 280 (2015).
- [10] J. Xiong, S. Kushwaha, J. Krizan, T. Liang, R. J. Cava, and N. P. Ong, *Europhys. Lett.* **114**, 27002 (2016).
- [11] H. F. Yuan, W. Xu, X. N. Zhao, D. Song, G. R. Zhang, Y. M. Xiao, L. Ding, and F. M. Peeters, *Phys. Rev. B* **99**, 235303 (2019).
- [12] C.-Z. Li, L.-X. Wang, H. W. Liu, J. Wang, Z.-M. Liao, and D.-P. Yu, *Nat. Commun.* **6**, 10137 (2015).
- [13] J. Xiong, S. K. Kushwaha, T. Liang, J. W. Krizan, M. Hirschberger, W. D. Wang, R. J. Cava, and N. P. Ong, *Science* **350**, 413 (2015).
- [14] S. Zhang, Q. Wu, L. Schoop, M. N. Ali, Y. Shi, N. Ni, Q. Gibson, S. Jiang, V. Sidorov, W. Yi, J. Guo, Y. Zhou, D. Wu, P. Gao, D. Gu, C. Zhang, S. Jiang, K. Yang, A. Li, Y. Li *et al.*, *Phys. Rev. B* **91**, 165133 (2015).
- [15] A. C. Lygo, B. H. Guo, A. Rashidi, V. Huang, P. Cuadros-Romero, and S. Stemmer, *Phys. Rev. Lett.* **130**, 046201 (2023).
- [16] W. Lu, S. F. Ge, X. F. Liu, H. Lu, C. Z. Li, J. W. Lai, C. Zhao, Z. M. Liao, and S. Jia, and D. Sun, *Phys. Rev. B* **95**, 024303 (2017).
- [17] D. Neubauer, J. P. Carbotte, A. A. Nateprov, A. Lohle, M. Dressel, and A. V. Pronin, *Phys. Rev. B* **93**, 121202(R) (2016).
- [18] L. Hou, Y. K. Yang, A. L. Li, Q. J. Wang, Q. N. Li, M. Wu, P. C. Ji, Y. J. Zhang, Y. M. Xiao, W. Xu, F. X. Xiu, and L. Ding, *Phys. Rev. B* **108**, 115416 (2023).
- [19] M. Uchida, Y. Nakazawa, S. Nishihaya, K. Akiba, M. Kriener, Y. Kozuka, A. Miyake, Y. Taguchi, M. Tokunaga, N. Nagaosa, Y. Tokura, and M. Kawasaki, *Nat. Commun.* **8**, 2274 (2017).
- [20] C. Zhang, Y. Zhang, X. Yuan, S. H. Lu, J. L. Zhang, A. Narayan, Y. W. Liu, H. Q. Zhang, Z. L. Ni, R. Liu, E. S. Choi, A. Suslov, S. Sanvito, L. Pi, H.-Z. Lu, A. C. Potter, and F. X. Xiu, *Nature (London)* **565**, 331 (2019).
- [21] N. P. Armitage, E. J. Mele, and A. A. Vishwanath, *Rev. Mod. Phys.* **90**, 015001 (2018).
- [22] A.-Q. Wang, X.-G. Ye, D.-P. Yu, and Z.-M. Liao, *ACS Nano* **14**, 3755 (2020).
- [23] G. S. Jenkins, C. Lane, B. Barbiellini, A. B. Sushkov, R. L. Carey, F. G. Liu, J. W. Krizan, S. K. Kushwaha, Q. Gibson, T.-R. Chang, H.-T. Jeng, H. Lin, R. J. Cava, A. Bansil, and H. D. Drew, *Phys. Rev. B* **94**, 085121 (2016).
- [24] O. V. Kotov and Yu. E. Lozovik, *Phys. Rev. B* **93**, 235417 (2016).
- [25] A. Thakur, R. Sachdeva, and A. Agarwal, *J. Phys.: Condens. Matter* **29**, 105701 (2017).
- [26] A. Politano, G. Chiarello, B. Ghosh, K. Sadhukhan, C.-N. Kuo, C. S. Lue, V. Pellegrini, and A. Agarwal, *Phys. Rev. Lett.* **121**, 086804 (2018).
- [27] J.-J. Zhu, S. M. Badalyan, and F. M. Peeters, *Phys. Rev. B* **87**, 085401 (2013).
- [28] J. H. Zhou, H.-R. Chang, and D. Xiao, *Phys. Rev. B* **91**, 035114 (2015).
- [29] S. Jeon, B. B. Zhou, A. Gyenis, B. E. Feldman, I. Kimchi, A. C. Potter, Q. D. Gibson, R. J. Cava, A. Vishwanath, and A. Yazdani, *Nat. Mater.* **13**, 851 (2014).
- [30] J. Z. Cao, S. H. Liang, C. Zhang, Y. W. Liu, J. W. Huang, Z. Jin, Z.-G. Chen, Z. J. Wang, Q. S. Wang, J. Zhao, S. Y. Li, X. Dai, J. Zou, Z. C. Xia, L. Li, and F. X. Xiu, *Nat. Commun.* **6**, 7779 (2015).
- [31] B. Zhou, H.-Z. Lu, R.-L. Chu, S.-Q. Shen, and Q. Niu, *Phys. Rev. Lett.* **101**, 246807 (2008).
- [32] A. Narayanan, M. D. Watson, S. F. Blake, N. Bruyant, L. Drigo, Y. L. Chen, D. Prabhakaran, B. Yan, C. Felser, T. Kong, P. C. Canfield, and A. I. Coldea, *Phys. Rev. Lett.* **114**, 117201 (2015).
- [33] Q. N. Li, W. Xu, Y. M. Xiao, L. Ding, B. Van Duppen, and F. M. Peeters, *J. Appl. Phys.* **128**, 155707 (2020).
- [34] M. Dressel, G. Gruener, and G. F. Bertsch, *Am. J. Phys.* **70**, 1269 (2002).
- [35] B. Wunsch, T. Stauber, F. Sols, and F. Guinea, *New J. Phys.* **8**, 318 (2006).
- [36] Q. S. Wang, C.-Z. Li, S. F. Ge, J.-G. Li, W. Lu, J. W. Lai, X. F. Liu, J. C. Ma, D.-P. Yu, Z.-M. Liao, and D. Sun, *Nano Lett.* **17**, 834 (2017).
- [37] M. Dadsetani and A. Ebrahimian, *J. Electron. Mater.* **45**, 5867 (2016).
- [38] X.-F. Wang and T. Chakraborty, *Phys. Rev. B* **75**, 033408 (2007).
- [39] H. M. Dong, L. L. Li, W. Y. Wang, S. H. Zhang, C. X. Zhao, and W. Xu, *Physica E* **44**, 1889 (2012).